The Astrophysical Journal, 902:29 (11pp), 2020 October 10 https://doi.org/10.3847/1538-4357/abb46e

Multifrequency Observations of the Candidate Neutrino-emitting Blazar BZB J0955+3551

Vaidehi S. Paliya[1], M. Böttcher[2], A. Olmo-García[3], A. Domínguez[4], A. Gil de Paz[4], A. Franckowiak[1], S. Garrappa[1], and R. Stein[1]
[1] Deutsches Elektronen Synchrotron DESY, Platanenallee 6, D-15738 Zeuthen, Germany; vaidehi.s.paliya@gmail.com
[2] Centre for Space Research, North-West University, Potchefstroom, 2531, South Africa
[3] Universidad Complutense de Madrid (UCM, Spain) and Instituto de Física de Partículas y del Cosmos (IPARCOS), Spain
[4] IPARCOS and Department of EMFTEL, Universidad Complutense de Madrid, E-28040 Madrid, Spain
Received 2020 March 19; revised 2020 August 25; accepted 2020 August 31; published 2020 October 8

Abstract

The recent spatial and temporal coincidence of the blazar TXS 0506+056 with the IceCube-detected neutrino event IC-170922A has opened up a realm of multimessenger astronomy with blazar jets as a plausible site of cosmic-ray acceleration. After TXS 0506+056, a second blazar, BZB J0955+3551, was recently found to be spatially coincident with the IceCube-detected neutrino event IC-200107A and undergoing its brightest X-ray flare measured so far. Here we present the results of our multifrequency campaign to study this peculiar event that includes observations with the NuSTAR, Swift, Neutron star Interior Composition Explorer (NICER), and 10.4 m Gran Telescopio Canarias (GTC). The optical spectroscopic observation from GTC secured its redshift as $z = 0.55703^{+0.00033}_{-0.00021}$ and the central black hole mass as $10^{8.90\pm0.16}\ M_{\odot}$. Both NuSTAR and NICER data reveal a rapid flux variability, albeit at low significance ($\lesssim 3.5\sigma$). We explore the origin of the target photon field needed for the photopion production using analytical calculations and considering the observed optical-to-X-ray flux level. We conclude that seed photons may originate from outside the jet, similar to that reported for TXS 0506+056, although a scenario invoking a comoving target photon field (e.g., electron synchrotron) cannot be ruled out. The electromagnetic output from the neutrino-producing photohadronic processes are likely to make only a subdominant contribution to the observed spectral energy distribution, suggesting that the X-ray flaring event may not be directly connected with IC-200107A.

Unified Astronomy Thesaurus concepts: Relativistic jets (1390); BL Lacertae objects (158); Neutrino astronomy (1100); X-ray active galactic nuclei (2035)

1. Introduction

High-energy neutrinos are unique messengers originating from the extreme physical processes in the universe. Being solely produced in hadronic interactions of high-energy cosmic-ray nuclei with ambient matter or photon fields, they provide the smoking-gun signature for hadronic acceleration sites.

Blazars, i.e., radio-loud quasars with powerful relativistic jets aligned to our line of sight, have been suggested as potential cosmic-ray and neutrino sources (see, e.g., Mannheim et al. 1992; Petropoulou et al. 2015; Murase 2017; Garrappa et al. 2019; Lucarelli et al. 2019; Franckowiak et al. 2020). The most compelling high-energy neutrino source candidate identified so far is the blazar TXS 0506+056 (IceCube Collaboration et al. 2018a, 2018b). The 290 TeV neutrino IC-170922A was found in spatial coincidence with TXS 0506 +056 and arrived during a major outburst observable in all wavelengths (IceCube Collaboration et al. 2018a). Interestingly, an archival search for lower-energy $\mathcal{O}(10\,\mathrm{TeV})$ neutrinos revealed a neutrino flare in 2014/15 that lasted 160 days but was not accompanied by activity in the electromagnetic regime (IceCube Collaboration et al. 2018b). From a theoretical perspective, Reimer et al. (2019) proposed that there should not be strongly correlated γ-ray and neutrino activity, and that neutrino production activity (through associated cascading) might actually show up more clearly in X-rays. However, the conclusion about the γ-ray/PeV neutrino correlation is reported to be model-dependent (see, e.g., Rodrigues et al. 2019; Zhang et al. 2020).

The BL Lacertae objects (or BL Lacs) are a subpopulation of blazars that exhibit an optical spectrum lacking any emission lines with an equivalent width >5 Å (e.g., Stickel et al. 1991). Their optical spectra are power-law–dominated, indicating either especially strong nonthermal continuum (due to Doppler boosting) or unusually weak thermal disk/broad-line emission (plausibly attributed to low accretion activity; Giommi et al. 2012). The BL Lacs that have a synchrotron peak located at very high frequencies ($\nu_{\rm syn}^{\rm peak} \geqslant 10^{17}$ Hz) are termed "extreme blazars" (e.g., Costamante et al. 2001; Foffano et al. 2019; Paliya et al. 2019a). The observation of such a high synchrotron peak frequency indicates that they host some of the most efficient particle accelerator jets. Interestingly, extreme blazars are also proposed as promising candidates of high-energy neutrinos (see Petropoulou et al. 2015; Padovani et al. 2016).

So far, any clustering of neutrinos in either space or time has not been confirmed in the all-sky searches of IceCube data (Aartsen et al. 2015, 2017a, 2020). Therefore, a promising methodology could be the search for transient and variable electromagnetic sources temporally and spatially coincident with IceCube neutrino events using multifrequency observations.

In this regard, the identification of a γ-ray-detected extreme blazar, BZB J0955+3551 (also known as 4FGL J0955.1 +3551), found in spatial coincidence with the IceCube-detected neutrino event IC-200107A (Giommi et al. 2020; IceCube Collaboration 2020; Krauss et al. 2020), has provided an interesting case for blazar jets as a plausible source of cosmic neutrinos. In fact, a prompt Swift X-ray Telescope (XRT) target-of-opportunity (ToO) observation of BZB J0955

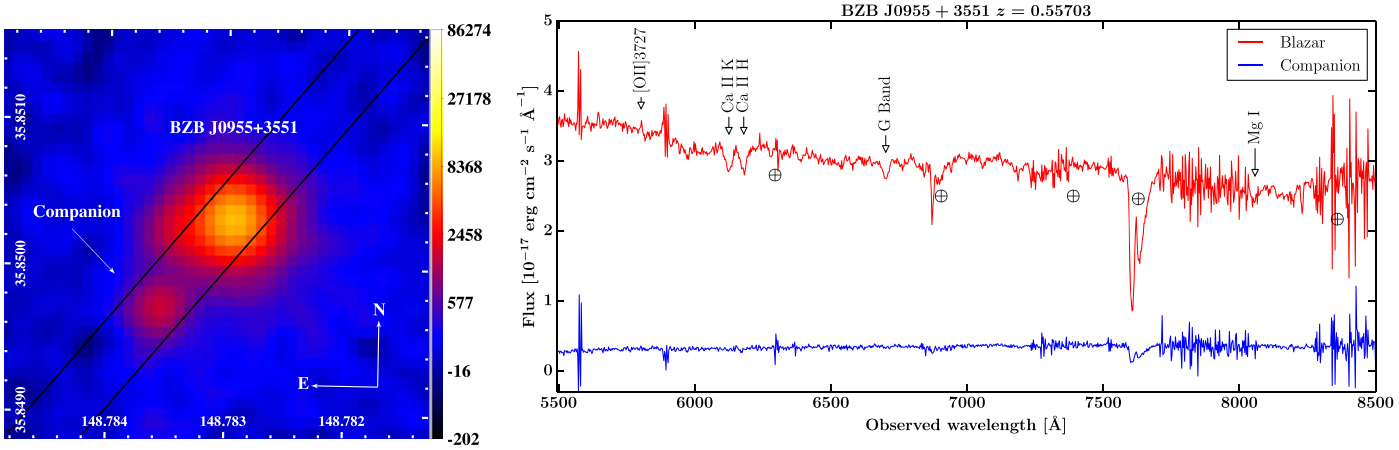

Figure 1. Left: Pan-STARRS i'-filter image of BZB J0955+3551. Note the presence of a faint companion object $\sim 3''$ southeast of the blazar. Parallel black lines represent the slit position for the long-slit spectrograph OSIRIS. The color bar represents the Pan-STARRS count units. Right: optical spectra of the source BZB J0955 +3551 and the companion taken at GTC with OSIRIS. The red line is the spectrum of the blazar, and the blue line is the spectrum of the companion. The identified emission and absorption lines are marked with vertical arrows and labeled correspondingly. The atmospheric absorption features are marked with the symbol $\oplus$.

+3551 on 2020 January 8 found it to be undergoing its brightest X-ray flare measured so far. Another γ-ray-detected blazar, 4FGL J0957.8+3423, was found to lie within the 90% positional uncertainty of IC-200107A; however, no significant flux enhancement was noticed from this object in X- or γ-rays (Garrappa et al. 2020; Krauss et al. 2020).

Motivated by the identification of a candidate neutrino-emitting blazar undergoing an X-ray outburst close in time to the neutrino arrival, we started a multiwavelength campaign. This includes a Director's Discretionary Time (DDT) observation with the Nuclear Spectroscopic Telescope Array (NuSTAR) and multiple Swift ToO observations. An optical spectroscopic follow-up with the 10.4 m Gran Telescopio Canarias (GTC) was carried out to determine the spectroscopic redshift of BZB J0955 +3551. In addition to that, the source was also observed with the Neutron star Interior Composition Explorer (NICER) simultaneous to the NuSTAR pointing as a part of the DDT ToO invoked by the mission principal investigator. Here we present the results of the conducted multifrequency campaign and attempt a theoretical interpretation to understand the underlying physical processes. In Section 2, we describe the steps adopted to analyze various data sets. The results are presented in Section 3 and discussed in Section 4. We summarize our findings in Section 5. Throughout, we adopt a cosmology of $H_0 = 67.8$ km s^{-1} Mpc^{-1}, $\Omega_m = 0.308$, and $\Omega_\Lambda = 0.692$ (Planck Collaboration et al. 2016).

2. Data Reduction and Analysis

2.1. Optical Spectroscopy with GTC

The i'-filter image of BZB J0955+3551 taken with the Panoramic Survey Telescope and Rapid Response System (Pan-STARRS) is shown in Figure 1. A faint companion object (i' magnitude $= 20.85 \pm 0.36$) located $\sim 3''$ southeast of the blazar (i' magnitude $= 19.17 \pm 0.06$) can be seen. Since both objects lacked spectroscopic redshift information, we carried out long-slit spectroscopy of the system with the Optical System for Imaging and low-Intermediate-Resolution Integrated Spectroscopy (OSIRIS; Cepa et al. 2000, 2003) spectrograph mounted at GTC.

The $0\farcs8$ wide slit was positioned to cover the source and a companion $\sim 3''$ southeast of the blazar (see Figure 1). The total integration time was $\sim$2 hr divided into six exposures of 1098 s each. The chosen grism was R1000R, which covers the spectral range of 5100–10000 Å with a resolution ($\lambda/\Delta\lambda$) of 1122.[5] This grism was selected due to its large spectral range and good spectral resolution, which provides a large pool to find emission or absorption lines and calculate the redshift of the source.

The raw data were reduced using the standard procedure with the IRAF tasks through the PyRAF software.[6] The main steps are bias and flat correction, cosmic-ray removal, wavelength calibration, sky subtraction, spectral extraction, and flux calibration. The cosmic rays were removed in each individual science spectrum with the IRAF task `lacos_spec` (van Dokkum 2001). The wavelength calibration was done with a combination of arcs from three different lamps (Hg–Ar, Ne, and Xe) to cover all of the wavelength range of the spectra. The sky was subtracted with the IRAF task `background`, selecting background samples to the right of the blazar and the left on the companion, and fitted with a Chebyshev polynomial of order 3. After this step, the science spectra were combined, which removed any cosmic-ray residual. The spectrum of the blazar and the companion were extracted independently from the combined science spectra. The extraction was done with the IRAF task `apall`, optimizing the apertures to extract the most flux from the sources. For the flux calibration, the spectrophotometric standard star G191-B2B was observed on the same night of the observation. This calibration included atmospheric extinction correction at the observatory (King 1985). Each spectrum was flux calibrated to convert from counts to absolute flux units and corrected from Galactic extinction using the IRAF task `deredden` with the values $R = 3.1$, $E(B-V) = 0.0109$ (Schlafly & Finkbeiner 2011).

2.2. NuSTAR, NICER, and Swift

NuSTAR observed BZB J0955+3551 on 2020 January 11 for a net exposure of 25.6 ks under our DDT request (ObsID 90501658002; PI: Paliya). We first cleaned and calibrated the

[5] http://www.gtc.iac.es/instruments/osiris/osiris.php

[6] PyRAF is a product of the Space Telescope Science Institute, which is operated by AURA for NASA; http://www.stsci.edu/institute/software_hardware/pyraf/.

event file using the tool `nupipeline`. We defined the source and background regions as circles of 30″ and 70″, respectively. The former was centered at the target blazar and the latter from a nearby region on the same chip and avoiding source contamination. The pipeline `nuproducts` was used to extract light curves, spectra, and ancillary response files. In the energy range of 3−79 keV, a binning of 1.5 ks was adopted to generate the light curve, and the source spectrum was binned to have at least 20 counts bin^{-1}.

NICER observed BZB J0955+3551 for a net exposure of ∼11 ks, simultaneous to the NuSTAR pointing on 2020 January 11 as a DDT ToO (ObsID 2200990102). We analyzed the NICER data with the latest software, HEASOFT 6.26.1, and calibration files (v. 20190516). In particular, the pipeline `nicerl2` was adopted with default settings to select all 56 detectors, apply standard filters and calibration to clean the events, and finally merge them to generate one event file. We then used the tool `xselect` to extract the source spectrum and 3 minute binned light curve. The background was estimated using the tool `nicer_bkg_estimator`[7] (K. Gendreau et al. 2020, in preparation). The quasar spectrum was binned to 20 counts bin^{-1}.

Close in time to the arrival of the IC-200107A neutrino, ToO observations of BZB J0955+3551 from the Swift satellite were carried out on 2020 January 8 (Giommi et al. 2020; Krauss et al. 2020), 10, and 11. We first cleaned and calibrated the XRT data taken in the photon-counting mode with the tool `xrtpipeline` and by adopting the latest CALDB (v. 20200106). Exposure maps and ancillary response files were generated with the tasks `ximage` and `xrtmkarf`, respectively. To extract the source spectrum, we considered a circular region of 47″, which encloses about 90% of the XRT point-spread function, centered at the target. The background was estimated from an annular region centered at the target with inner and outer radii of 70″ and 150″, respectively. We binned the blazar spectrum to 20 counts bin^{-1}. The X-ray spectral analysis was carried out in XSPEC (Arnaud 1996), and the Galactic neutral hydrogen column density ($N_{\rm H} = 1.14 \times 10^{20}$ cm^{-2}) was adopted from Kalberla et al. (2005).

Individual snapshots taken from the Swift UltraViolet Optical Telescope (UVOT) were first combined using the pipeline `uvotimsum`, and then photometry was performed with the task `uvotsource`. For the latter, we considered a source region of 2″, avoiding the nearby object located ∼3″ southeast of BZB J0955+3551. The background is estimated from a 30″ circular region free from the source contamination. The derived magnitudes were corrected for Galactic extinction (Schlafly & Finkbeiner 2011) and converted to flux units following zero-points adopted from Breeveld et al. (2011).

2.3. Others

The object BZB J0955+3551 remained below the detection threshold of the Fermi Large Area Telescope (LAT) at the time of the neutrino arrival and prior on a month-to-years timescale (Garrappa et al. 2020). Therefore, we used the spectral parameters provided in the recently released fourth catalog of the Fermi-LAT–detected objects (4FGL; Abdollahi et al. 2020) to get an idea of the average γ-ray behavior of the source. In addition to that, we used archival measurements from the Space Science Data Center.[8] These data sets can provide meaningful information about the typical activity state of the source.

2.4. Probability of Chance Coincidence

The third catalog of high synchrotron peaked blazars (3HSP; Chang et al. 2019) contains 384 extreme blazars, yielding a density of 9.3×10^{-3} deg^{-2} of sky. Since the total number of extreme blazars is predicted to be ∼400 (Chang et al. 2019), the sample of extreme blazars present in the 3HSP catalog can be considered almost complete. Given that IC-200107A had a 90% localization of 7°.6, we thus expect to find 7.1×10^{-2} extreme blazars coincident with the neutrino.

We can additionally determine the X-ray flare rate or duty cycle (DC) for extreme blazars, as for any other class of astrophysical objects, using the X-ray variability information collected from an all-sky surveying instrument. For this, we used publicly available 2−12 keV light curves generated using the data from the All Sky Monitor (ASM) on board the Rossi X-ray Timing Explorer (RXTE) mission.[9] We cross-matched the RXTE ASM catalog of 587 sources with 3HSP and found ASM light curves for 17 extreme blazars. To avoid spurious detection due to poor sensitivity of the instrument, for each object, we considered only data points that qualified the following two filters: (i) the count rate ($R_{\rm ASM}$) should be positive, and (ii) $R_{\rm ASM}/\Delta R_{\rm ASM} > 2$, where $\Delta R_{\rm ASM}$ is the 1σ uncertainty in $R_{\rm ASM}$. Furthermore, the observation on a particular day was considered a flare if the count rate estimated for that day of observation ($R_{\rm ASM,i}$) fulfilled the following condition:

$$R_{\rm ASM,i} - \Delta R_{\rm ASM,i} \geqslant 2 \times \langle R_{\rm ASM} \rangle, \quad (1)$$

where $\langle R_{\rm ASM} \rangle$ is the median count rate for the mission light curve. If the observation on a particular day qualified the abovementioned filter (Equation (1)), we flagged it as a "flare," otherwise it is a "nonflare." The DC is then computed as the ratio of the number of flaring epochs divided by total observing epochs. This exercise led to a mean DC for the sample of 5.2% with a range of 1.7%–8.9%. Assuming the mean DC of these 17 extreme blazars is representative of the broader extreme blazar population, the probability of finding a coincident extreme blazar by chance that is simultaneously flaring in X-rays is just 3.7×10^{-3}. This estimate is, however, specific to IC-200107A. The possibility that other high-energy neutrinos may have had flaring extreme blazar counterparts is difficult to quantify without a systematic follow-up program.

2.5. Neutrino Flux Estimate

A single high-energy neutrino detection from the extreme blazar population would suggest a cumulative expectation of $0.05 < N_{\rm pop} < 4.74$ at 90% confidence, with each of the 384 extreme blazars contributing some fraction of this total (Strotjohann et al. 2019). If each had an equal likelihood of generating a neutrino alert, we would expect $1.3 \times 10^{-4} \lesssim N_{\rm src} \lesssim 0.012$ per extreme blazar.

Given that the association with BZB J0955+3551 is not dependent on the event topology of IC-200107A, we simply require sufficient neutrino flux for a single high-energy

[7] https://heasarc.gsfc.nasa.gov/docs/nicer/tools/nicer_bkg_est_tools.html

[8] https://tools.ssdc.asi.it/

[9] http://xte.mit.edu/ASM_lc.html

neutrino alert under any of the public IceCube real-time alert selections. The event IC-200107A was identified by a new neural network classifier (IceCube Collaboration 2020) that identifies high-energy starting track events with high efficiency (Kronmueller & Glauch 2019). However, with an overall rate of high-energy starting tracks that is just ~ 2 yr^{-1} (IceCube Collaboration 2020), the effective area for this selection is still substantially smaller than that for throughgoing muon alerts (Blaufuss et al. 2019).

We can derive the necessary neutrino fluence normalization by taking the sum of the neutrino effective areas at the decl. of BZB J0955+3551 over the duration of the IceCube real-time system. For this 4 yr period, which overlaps a transition in IceCube event selections, we integrate each effective area over the period that it was active (Aartsen et al. 2017b; Blaufuss et al. 2019). No neutrino energy estimate was provided for IC-200107A (IceCube Collaboration 2020), so we here assume an approximate neutrino energy of $\sim$100 TeV, the energy at which most starting tracks are expected for an E^{-2} spectrum. The effective area at this energy was 0.7 m^2 under the old alert selection (Aartsen et al. 2017b) and 9.48 m^2 under the new alert selection (Blaufuss et al. 2019), yielding a weighted average of 2.9 m^2 at the decl. of the source. With this effective area, at 100 TeV, we require a mean neutrino flux of 6×10^{-15} erg cm^{-2} s^{-1} $< F_{\rm steady} < 5 \times 10^{-13}$ erg cm^{-2} s^{-1} for extreme blazars such as BZB J0955+3551. If we assume that neutrino emission from these sources is dominated by X-ray flares, then for a DC of 5.2%, we expect a flux of 1×10^{-13} erg cm^{-2} s^{-1} $< F_{\rm flare} < 1 \times 10^{-11}$ erg cm^{-2} s^{-1} for the duration of each flare. Given the large range of the expected neutrino flux, we conservatively assume a value of 10^{-13} erg cm^{-2} s^{-1} for rest of the calculation, considering an Eddington bias of a factor of 100 (Strotjohann et al. 2019).

3. Results

The optical spectra of BZB J0955+3551 and the nearby companion are shown in Figure 1. Various absorption lines associated with the host galaxy, e.g., the Ca II H&K doublet, are identified in the optical spectrum of the blazar. Additionally, we also detected a weak [O II] 3727 emission line. These allowed us to firmly establish the redshift of BZB J0955+3551 as $z = 0.55703^{+0.00033}_{-0.00021}$. The spectrum of the companion does not reveal any noticeable feature. Deeper spectroscopic observations are necessary to characterize this object and explore the possibility of its interaction/merger with BZB J0955+3551.

We computed the rest-frame equivalent width of the [O II] 3727 emission line by fitting the continuum around the emission line with a polynomial of degree 1 and the emission line with a Gaussian function (see top left panel in Figure 2). The data were normalized by the factor 10^{-17}. We first fitted the continuum with a sample of 45 points $\sim$30 and $\sim$40 Å to either side of the line. With the continuum subtracted from the spectrum, we fitted the emission line using seven points ($\sim$11 Å), more than the three free parameters in the fit. This leads to a rest-frame equivalent width of 0.15 ± 0.05 Å and line luminosity as $(6 \pm 2) \times 10^{39}$ erg s^{-1}. Note that the signal-to-noise ratio around the [O II] 3727 line is >70, which ensures that the estimated values are reliable. Moreover, during the analysis, we varied the extraction aperture, which changed the amount of sky residuals in the final spectrum, to determine if the observed emission line could be due to background noise. In all cases, the line was clearly visible. Therefore, we conclude that the line detection is real and free from any artifacts.

In order to ascertain the impact of the background on the NICER observation, we plot the count spectrum of the source and background in Figure 2 (top right panel). As can be seen, the NICER spectrum remains source-dominated up to $\sim$5 keV. Therefore, we used the 0.3−5 keV energy range to extract the NICER light curve and spectrum of BZB J0955+3551.

In the bottom left panel of Figure 2, we show the NICER and NuSTAR light curves. The light curves are scanned to search for rapid flux variations. This was done by computing the flux doubling/halving time (τ) as follows:

$$F(t_2) = F(t_1) 2^{(t_2 - t_1)/\tau}, \quad (2)$$

where $F(t_1)$ and $F(t_2)$ are the fluxes at time t_1 and t_2, respectively. The uncertainties in the flux values were taken into account by setting the conditions that the difference in fluxes at epochs t_1 and t_2 is at least 2σ significant.

We found evidence of rapid flux variations in the NICER data with the shortest flux halving time of 28.3 ± 7.9 minutes at a 3.5σ significance level. The NuSTAR light curve also revealed traces of fast variability with the shortest flux doubling time of 19.2 ± 10.7 minutes, albeit at a low 2.2σ confidence level.

In order to search for curvature in the X-ray spectrum, we fitted two models, a power law and a log-parabola, taking into account the Galactic absorption. The goodness of the fit was determined using the F-test. The results of the spectral analysis are provided in Table 1, and the residuals of the fit are shown in Figure 2 (bottom right panel). The XRT spectrum taken on January 8 is well explained with a simple absorbed power-law model, whereas that of January 10 is better fit with the log-parabola model. The joint NICER and NuSTAR spectrum from January 11 is also well explained with an absorbed log-parabola model, clearly revealing the synchrotron peak. Note that we do not use Swift-XRT data in the January 11 spectral fitting for two reasons: (i) the fit is dominated by NICER and NuSTAR spectra because of much better photon statistics, and (ii) after removing bad channels (using the `ignore bad` command in XSPEC), the Swift-XRT spectrum is limited up to 5 keV, thus giving no advantage over the NICER observation.

The broadband spectral energy distribution (SED) of BZB J0955+3551 during the January 8, 10, and 11 epochs is shown in Figure 3. The archival IR–optical spectrum reveals a bump that likely originated from the host galaxy and has been noticed in many extreme blazars (see, e.g., Costamante et al. 2018). The long time-averaged 4FGL SED reveals an extremely hard γ-ray spectrum suggesting that the inverse Compton peak is located at very high energies (VHEs; >100 GeV). Note that at this redshift, the extragalactic background light attenuation is also significant (Domínguez et al. 2011; Paliya et al. 2019a).

4. Discussion

4.1. Properties of the Central Engine

We have used the well-calibrated empirical relation between the black hole mass ($M_{\rm BH}$) and the central stellar velocity dispersion (σ_*) to determine the former (see Gültekin et al. 2009; Kormendy & Ho 2013). To determine σ_*, we used the penalized PiXel Fitting software (`pPXF`; Cappellari &

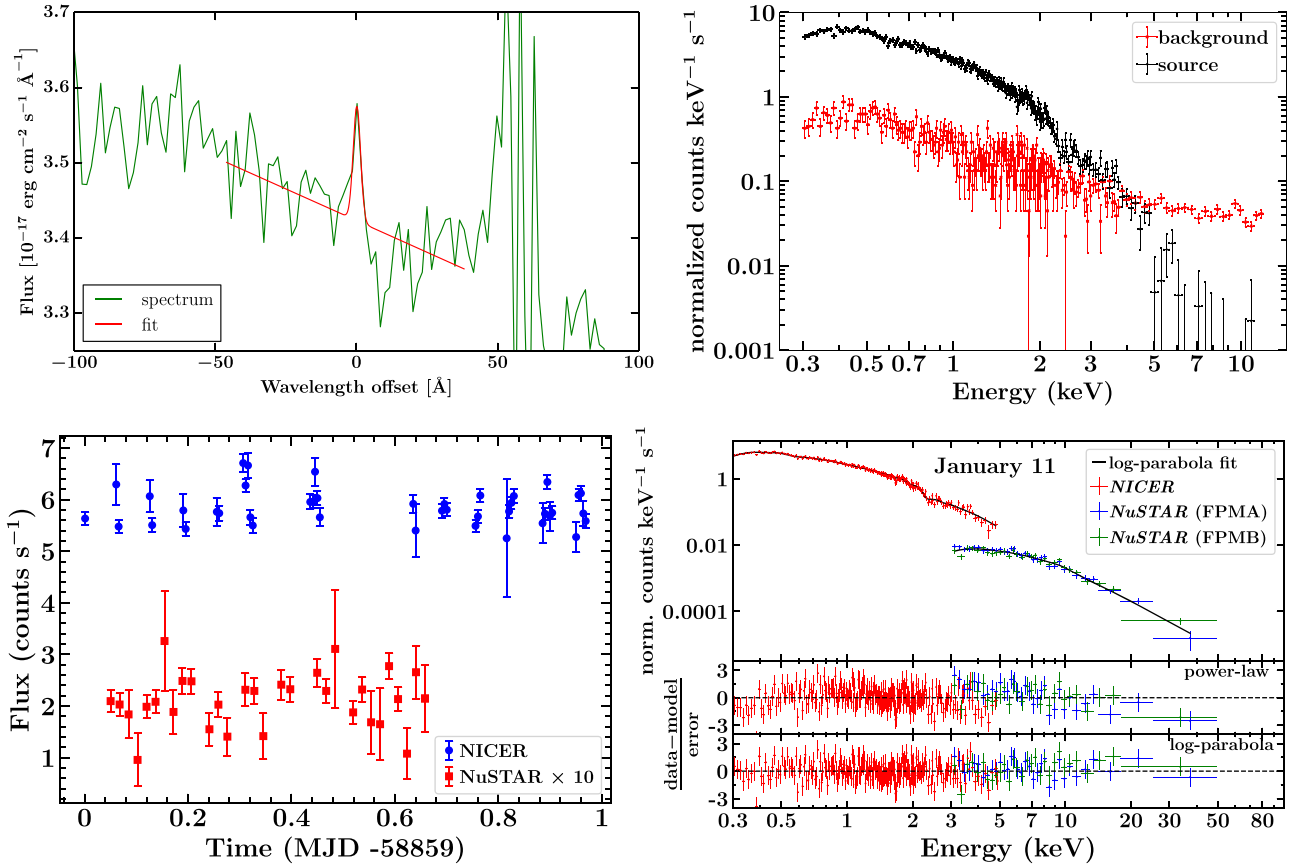

Figure 2. Top left: fit of the emission line [O II] 3727 to derive its luminosity and equivalent width. The spectrum is shown with a green line and the fit with a red line. The continuum is fit with a polynomial of degree 1 and the line with a single Gaussian function. The wavelength of the line has been subtracted from the *x*-axis. Top right: NICER count spectra of BZB J0955+3551 (black) and the background (red). As can be seen, at $\gtrsim$5 keV, the background dominates the observed counts. Bottom left: 1.5 ks binned NuSTAR (3−79 keV) and 3 minute binned NICER (0.3−5 keV) light curves of BZB J0955+3551. The flux of the former is multiplied by 10 for a meaningful comparison. Bottom right: NICER and NuSTAR count spectra jointly fitted with the best-fit log-parabola model. The lower panels show the residuals of the fit for two models: power law and log-parabola, as labeled.

Emsellem 2004). This tool works in pixel space and adopts a maximum penalized likelihood approach to derive the line-of-sight velocity distribution (LOSVD) from kinematic data (Merritt 1997). To fit the galaxy spectrum, pPXF uses a large set of single stellar population spectral libraries that we adopted from Vazdekis et al. (2010). It first creates a template galaxy spectrum by convolving the stellar population models with the parameterized LOSVD and then fits the model on the observed galaxy spectrum by minimizing χ^2. We also added a fourth-order Legendre polynomial to account for the likely featureless contribution from the nuclear emission. From the best-fit spectrum, pPXF computes σ_* and associated 1σ uncertainty. The result of this analysis is shown in Figure 4, and the derived σ_* is 306.04 $\pm$ 18.71 km s^{-1}.

We used the following empirical relation to compute $M_{\rm BH}$ (Gültekin et al. 2009):

$$\log\left(\frac{M_{\rm BH}}{M_\odot}\right) = (8.12 \pm 0.08) + (4.24 \pm 0.41) \times \log\left(\frac{\sigma_*}{200\ {\rm km\ s^{-1}}}\right). \quad (3)$$

By supplying the σ_* derived from the pPXF fit in the above equation, the mass of the central black hole is obtained as $\log M_{\rm BH,\odot} = 8.90 \pm 0.16$. The quoted uncertainty is statistical only and does not include the intrinsic scatter ($\sim$0.4 dex) associated with this method (Gültekin et al. 2009).

Since no broad emission lines are detected in the optical spectrum of BZB J0955+3551, we have determined a 3σ upper limit on the broad-line region (BLR) luminosity ($L_{\rm BLR}$) by adopting the following procedure. The OSIRIS spectrum was analyzed in the rest-frame wavelength range [4700, 5000] Å, where the H β emission line is expected to be present. We brought the spectrum to the rest frame and fitted with a power law to reproduce the continuum. We assumed the Hβ emission line as a Gaussian with variable luminosity while keeping its FWHM fixed to 4000 km s^{-1}, a value typical for blazars (see Shaw et al. 2012). Then, a χ^2 test was performed by fitting the Gaussian model on the data by varying the line luminosity ($L_{\rm H\beta}$). We computed the upper limit to $L_{\rm H\beta}$ when $\chi^2 > \chi^2$ (99.7%), i.e., at a 3σ confidence level. The derived upper limit on $L_{\rm H\beta}$ is 1.1×10^{42} erg s^{-1}. This is demonstrated in the bottom panels of Figure 4. Furthermore, by adopting the line flux ratios from Francis et al. (1991) and Celotti et al. (1997), we estimated the $L_{\rm BLR}$ upper limit as $\sim 2.7 \times 10^{43}$ erg s^{-1}. The presence of a more luminous BLR can be ruled out, as that would emit stronger emission lines that should be observed in the optical spectrum. Furthermore, the inferred $L_{\rm BLR}$ implies an accretion rate (in Eddington units) of $L_{\rm BLR}/L_{\rm Edd} \lesssim 0.0003$.

Table 1
Summary of the SED Analysis

Epoch	Γ_X/α	β	Normalization	X-Ray Flux	χ^2/dof	Prob.	Instrument
Jan 8	$1.74^{+0.11}_{-0.10}$	⋯	$14.11^{+1.03}_{-1.03}$	$5.37^{+0.97}_{-0.77}$	22.93/27	0.6	Swift-XRT
Jan 10	$2.83^{+0.44}_{-0.38}$	$1.10^{0.54}_{0.49}$	$1.17^{+0.21}_{-0.22}$	$1.89^{+0.67}_{-0.48}$	14.07/21	$<10^{-4}$	Swift-XRT
Jan 11	$2.13^{+0.04}_{-0.04}$	$0.17^{+0.04}_{-0.03}$	$1.74^{+0.08}_{-0.07}$	$3.80^{+0.14}_{-0.17}$ $2.11^{+0.21}_{-0.15}$	456.94/462	$<10^{-4}$	NICER+NuSTAR

Epoch	Swift-UVOT *V*	*B*	*U*	*UVW1*	*UVM2*	*UVW2*
Jan 8	⋯	⋯	⋯	⋯	5.75 ± 0.56	6.03 ± 0.54
Jan 10	3.78 ± 1.24	3.13 ± 0.70	4.03 ± 0.59	4.58 ± 0.58	5.54 ± 0.55	6.23 ± 0.70
Jan 11	⋯	3.54 ± 0.72	3.91 ± 0.58	5.20 ± 0.72	5.36 ± 0.51	6.75 ± 0.74

Note. Swift-XRT spectral fitting (January 8 and 10) is done in the energy range of 0.3−10 keV, whereas it is 0.3−79 keV for the joint NICER and NuSTAR analysis (January 11). Here Γ_X is the power-law X-ray photon index, and α and β are the log-parabolic photon index at the pivot energy (fixed at 3 keV) and the curvature around the peak, respectively. The X-ray normalization has units of 10^{-4} ph cm^{-2} s^{-1} keV^{-1}. The quoted flux values are in the 2−10 keV energy range, and in the second row of January 11 data, we also provide the flux in 10−79 keV. The power-law and log-parabola models were compared by adopting the F-test, and the derived probability of the null hypothesis (that the power-law model is a better representation of the data) is given in the column "Prob." The flux values reported for the Swift-UVOT filters are in 10^{-13} erg cm^{-2} s^{-1} and corrected for Galactic reddening.

Such a low accretion rate suggests a radiatively inefficient accretion process and is expected in BL Lacs.

4.2. General Theoretical Considerations

The following section considers general energetic requirements for the production of a detectable IceCube neutrino flux in the jet of BZB J0955+3551. These are constrained by the observed UV–X-ray flux just after the detection of the neutrino event on 2020 January 8 and are similar to that reported for neutrino production in TXS 0506+056 by Reimer et al. (2019). Specifically, a flux around $\sim 10^{16}$–10^{17} Hz of $\nu F_\nu^{\rm UV\text{-}X} \sim 10^{-12}\, F_{\rm UV,-12}$ erg cm^{-2} s^{-1} was observed, while the peak of the X-ray spectrum was located around $\sim 10^{18}$ Hz at a flux close to $\nu F_\nu \sim 3 \times 10^{-12}$ erg cm^{-2} s^{-1} $\equiv 10^{-12}\, F_{X,-12}$ erg cm^{-2} s^{-1} with $F_{X,-12} \sim 3$. We first derive a general constraint on the jet content of protons that might potentially be responsible for VHE neutrino production and then consider two possibilities for the source of the target photons for photopion production on those protons.

The neutrino emission region propagates along the jet with a Lorentz factor $\Gamma = 10\,\Gamma_1$, leading to Doppler boosting characterized by a Doppler factor $D = 10\,D_1$. The observed subhour-scale X-ray variability suggests a size of the X-ray emission region of $R_X \lesssim 3.5 \times 10^{14}\, D_1$ cm. As our analytical and numerical modeling results below will demonstrate, it is unlikely that the observed X-ray emission has been produced in the same (photohadronic and cascade) processes as the neutrino emission. Hence, the neutrino emission region may be different from that producing X-rays. Assuming a neutrino emission region of the size mentioned above would lead to an unrealistically high compactness, with the required relativistic proton pressure exceeding the magnetic pressure by many orders of magnitude. For example, the assumed production of the observed neutrino flux through photopion processes requires characteristic proton powers of $L_{\rm p} \sim 10^{48}$–10^{49} erg s^{-1}. Writing $L_{\rm p} = 10^{48} L_{48}$ erg s^{-1}, the energy density in relativistic protons is then $u_{\rm p}^{'} \sim 10^3 L_{48}/(R_{16}^2)$ erg cm^{-3}, assuming a proton escape timescale of $t_{\rm esc}^{'} = 10^7$ s (see Böttcher et al. 2013, for details). Assuming relativistic protons, the pressure exerted by protons is $p_{\rm p}^{'} \sim u_{\rm p}^{'}/3 \sim 350 L_{48}/(R_{16}^2)$ dyne cm^{-2}. The magnetic pressure, on the other hand, is $p_{\rm B}^{'} \sim 400 B_2^2$ dyne cm^{-2}. Thus, for an emission region size $\ll 10^{16}$ cm, the proton pressure will exceed the magnetic pressure for any plausible value of the magnetic field. Thus, confinement of the emission region in such a small volume appears implausible. We therefore assume that neutrinos are produced in a larger emission region of size $R \sim 10^{16}\, R_{16}$ cm. In the following, primes denote quantities in the rest frame of this emission region. The redshift of $z = 0.5573$ corresponds to a luminosity distance of $d_L \sim 3.2$ Gpc $\sim 9.7 \times 10^{27}$ cm.

4.3. Proton–Photon Interactions and Neutrino Production

In active galactic nucleus (AGN) jets, neutrinos are most plausibly produced through photohadronic interactions of relativistic protons of energy $E_p^{'} = \gamma_p\, m_p c^2$ with target photons of energy $E_t^{'}$. This interaction is most efficient when the center-of-momentum frame energy squared, $s = (m_p c^2)^2 + 2\, E_p^{'}\, E_t^{'}\, (1 - \beta_p \cos\theta)$—where $\beta_p = \sqrt{1 - 1/\gamma_p^2}$ is the normalized velocity (in units of the speed of light c) and γ_p is the Lorentz factor of the proton—of the interaction is near the Δ^+ resonance, $s \sim E_{\Delta^+}^2 = (1232\ {\rm MeV})^2$, where the $p\gamma$ interaction cross section peaks. This translates into a condition $E_p^{'}\, E_t^{'} \sim 3.2 \times 10^5\ {\rm MeV}^2$.

The proton energy required to produce neutrinos at observed (i.e., Doppler-boosted) energies of hundreds of TeV, $E_\nu \equiv 100\, E_{14}$ TeV (E_{14} is the neutrino energy in units of 10^{14} eV), is $E_p^{'} \simeq 200\, E_{14}/(D_1\, \xi_{0.05})$ TeV (i.e., $\gamma_p^{'} = E_p^{'}/m_p c^2 \simeq 2 \times 10^5\, E_{14}/(D_1\, \xi_{0.05})$), where $\xi \equiv 0.05\, \xi_{0.05}$ is the average neutrino energy per initial proton energy in photohadronic interactions (Mücke et al. 1999). The Larmor radius of protons with such energy is $r_L \sim 6.7 \times 10^{10} (\gamma_p^{'}/[2 \times 10^5]) B_2^{-1}$ cm, where $B = 100\, B_2$ G is the magnetic field. This indicates that they are expected to be well confined within the emission region and can plausibly be accelerated by standard mechanisms.

For photopion (and neutrino) production by protons of this energy at the Δ^+ resonance, target photons of $E_t^{'} \geqslant 1.6 D_1 \xi_{0.05}/E_{14}$ keV are required. In Section 4.5, we will discuss two extreme options for the source of such target

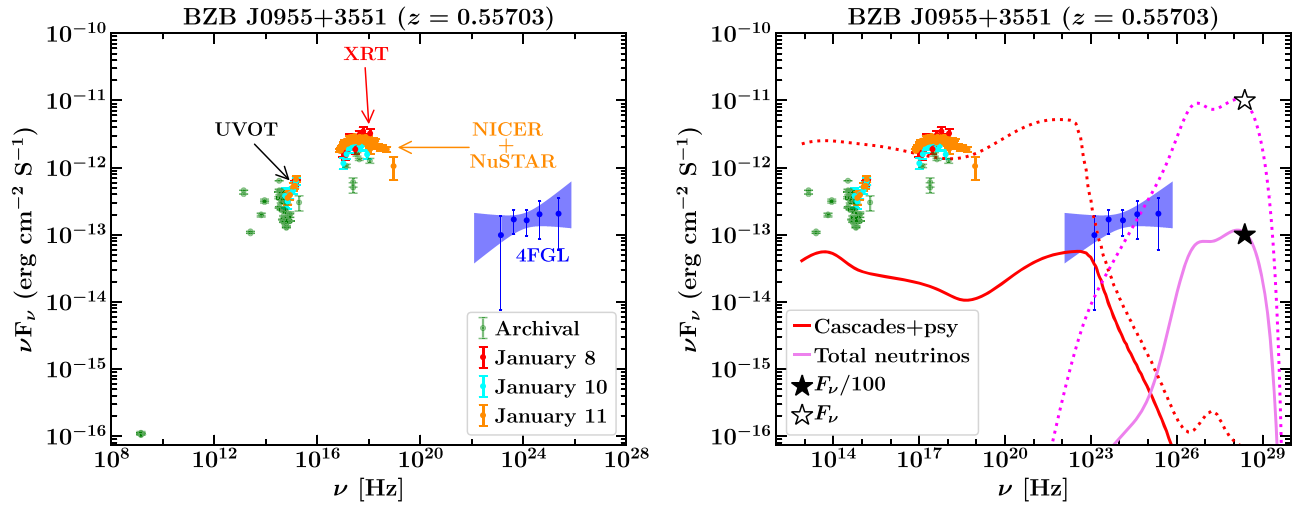

Figure 3. Left: broadband SED of BZB J0955+3551 generated using the data acquired on January 8 (red) and 11 (yellow) and also considering archival observations (green). In the Fermi-LAT energy range, we show the bow-tie and spectral data points adopted from the 4FGL catalog. Right: same as the left panel but plotting the results of the hadronic simulation performed using the parameters constrained from the observed optical-to-X-ray spectrum and derived from the analytical calculations in Section 4.2. We divide the expected 100 TeV neutrino flux of 1×10^{-11} erg cm^{-2} s^{-1} (black open star) by a factor of 100 (black filled star) to take into account the Eddington bias (see Strotjohann et al. 2019).

photons: (a) the comoving electron synchrotron radiation field and (b) an external radiation field that is isotropic in the AGN rest frame. First, however, we derive constraints on the number of relativistic protons that may be present in the jet.

4.4. Constraints on Jet Power

Protons of energy $E'_p = 200\, E_{14}/(D_1\, \xi_{0.05})$ TeV radiate proton synchrotron radiation at a characteristic frequency of

$$\nu^{\rm obs}_{\rm psy} = 4.2 \times 10^6\, B_G\, \gamma_p^2\, D (m_e/m_p)\ {\rm Hz}$$

$$\approx 9.2 \times 10^{16}\, \frac{B_2\, E_{14}^2}{D_1\, \xi_{0.05}^2}\ {\rm Hz}, \quad (4)$$

i.e., in soft X-rays. Given a number of protons of energy γ_p, i.e., $N_p(\gamma_p) \sim \gamma_p\, dN_p(\gamma_p)/d\gamma_p$, one may calculate the produced comoving luminosity in proton synchrotron radiation as

$$L'_{\rm psy} \approx \frac{c\, \sigma_T\, B^2}{6\pi}\left(\frac{m_e}{m_p}\right)^2 \gamma_p^3\, \frac{dN_p(\gamma_p)}{d\gamma_p}$$

$$\approx 2.5 \times 10^{-2}\, \frac{dN_p(\gamma_p)}{d\gamma_p}\, B_2^2\, \frac{E_{14}^3}{D_1^3\, \xi_{0.05}^3}\ {\rm erg\ s^{-1}}. \quad (5)$$

The resulting observable soft X-ray flux, $\nu F_\nu^{\rm psy} \sim D_1^4\, L'_{\rm psy}/(4\,\pi\, d_L^2)$, may not overshoot the actually observed UV–soft X-ray flux, thus constraining the differential number of protons to

$$\frac{dN_p(\gamma_p)}{d\gamma_p} \lesssim 4.7 \times 10^{42}\, \frac{F_{X,-12}\, \xi_{0.05}^3}{B_2^2\, D_1\, E_{14}^3}. \quad (6)$$

We consider a proton spectrum of the form $N_p(\gamma_p) = N_0\, \gamma_p^{-\alpha_p}$ with $\alpha_p = 2$, extending from $\gamma_{\rm p,min} = 1$ to $\gamma_{\rm p,max} \sim 2 \times 10^5\, E_{14}/(D_1\, \xi_{0.05})$ so that the resulting proton synchrotron spectrum actually peaks (in νF_ν representation) at the characteristic proton synchrotron frequency $\nu_{\rm psy}$ evaluated in Equation (4) above. The proton spectrum normalization is then constrained to

$$N_0 \lesssim 1.9 \times 10^{53}\, \frac{F_{X,-12}\, \xi_{0.05}}{B_2^2\, D_1^3\, E_{14}}, \quad (7)$$

limiting the kinetic jet power in relativistic protons to

$$L_p \sim \frac{3\, \Gamma^2\, c (m_p c^2) N_0}{4\, R}\, \ln \gamma_{\rm p,max}$$

$$\lesssim 6.4 \times 10^{46}\, \frac{F_{X,-12}\, \xi_{0.05}\, \Gamma_1^2}{B_2^2\, D_1^3\, E_{14}\, R_{16}} (12.2 + \eta)\ {\rm erg\ s^{-1}}, \quad (8)$$

where $\eta \equiv \ln(E_{14}/[D_1\, \xi_{0.05}])$. For $\eta = 0$ and all baseline parameters, Equation (8) evaluates to 2.3×10^{48} erg s^{-1} for a one-sided jet. In the following, we ignore the (presumed small) correction arising from potential values of $\eta \neq 0$.

Using the proton spectrum with the normalization given by Equation (7), we may estimate the comoving neutrino luminosity through the proton energy loss rate due to photopion production given by Kelner & Aharonian (2008; see also Berezinskii & Grigor'eva 1988; Stanev et al. 2000),

$$\dot{\gamma}_{\rm p,p\gamma} \approx -c\, \langle \sigma_{p\gamma} f \rangle\, n'_{\rm ph}(\epsilon'_t)\, \epsilon'_t\, \gamma_p, \quad (9)$$

where $\epsilon'_t = E'_t/(m_e c^2)$ and $\langle \sigma_{p\gamma} f \rangle \approx 10^{-28}$ cm^2 is the elasticity-weighted $p\gamma$ interaction cross section. The factor $n'_{\rm ph}(\epsilon'_t)\epsilon'_t$ provides a proxy for the comoving energy density of the target photon field, $u'_{\rm t} \approx m_e c^2\, n'_{\rm ph}(\epsilon'_t)(\epsilon'_t)^2$. Considering that the energy lost by protons in $p\gamma$ interactions is shared approximately equally between photons and neutrinos, the VHE neutrino luminosity is given by

$$L'_\nu \approx \frac{1}{2}\, N_0\, m_p c^2 \int_{\gamma_1}^{\gamma_{\rm p,max}} \gamma_p^{-2} |\dot{\gamma}_{\rm p,p\gamma}|\, d\gamma_p$$

$$\approx \frac{1}{2}\, c\, N_0\, m_p c^2\, \langle \sigma_{p\gamma} f \rangle\, \frac{u'_t}{\epsilon'_t\, m_e c^2}\, \ln\left(\frac{\gamma_{\rm p,max}}{\gamma_1}\right). \quad (10)$$

Considering that the target photon is unlikely to be monoenergetic, we set the lower limit in the integral in Equation (10) to $\gamma_1 = 6.4 \times 10^4/(D_1\, \xi_{0.05})$, corresponding to

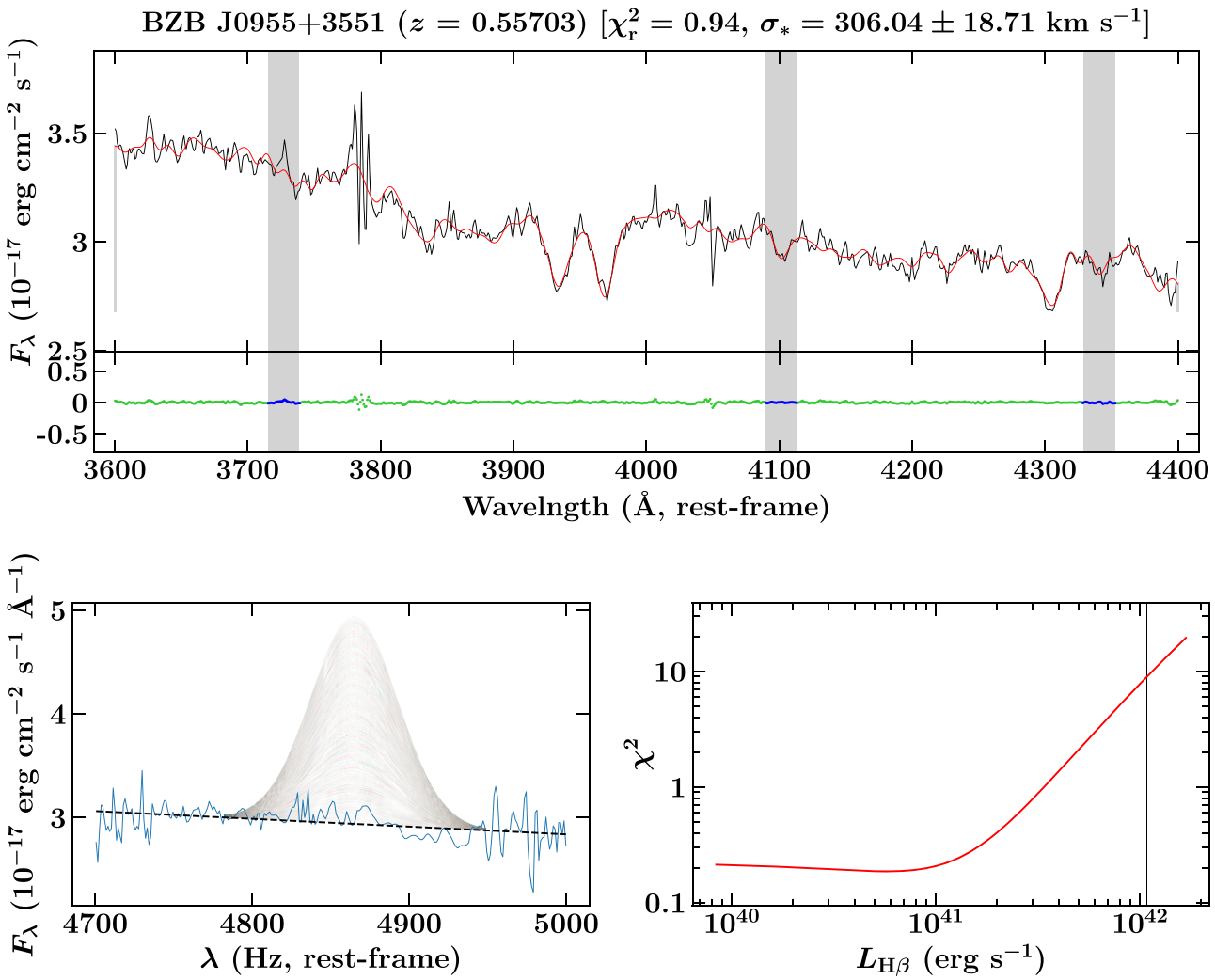

Figure 4. Top: optical spectrum of BZB J0955+3551 (black line) fitted with the stellar population synthesis tool pPXF (red line). The bottom panel refers to the residual of the fit. The gray shaded areas denote the wavelength regions excluded from the fit to mask emission lines. The derived stellar velocity dispersion and reduced χ^2 are quoted. Bottom: rest-frame OSIRIS spectrum (blue solid line, left panel) when fitted with a power law (black dashed line) and a single Gaussian function with variable $L_{H\beta}$. The right panel shows the variation of the derived χ^2 as a function of $L_{H\beta}$. The vertical black solid line highlights the $L_{H\beta}$ value beyond which $\chi^2 > \chi^2$ (99.7%).

protons producing neutrinos with an observed energy of ∼30 TeV. With this choice, the limit on the neutrino luminosity (corresponding to the limit on N_0 from Equation (7)) evaluates to

$$L'_\nu \lesssim 1.7 \times 10^{41} \frac{u'_t}{\mathrm{erg\ cm^{-3}}} \ln(3.1\,E_{14}) \frac{F_{X,-12}}{B_2^2\,D_1^4}\ \mathrm{erg\ s^{-1}}, \quad (11)$$

which yields a limit on the VHE neutrino flux measured on Earth as

$$F_\nu \lesssim 1.4 \times 10^{-12} \frac{u'_t}{\mathrm{erg\ cm^{-3}}} \ln(3.1\,E_{14}) \frac{F_{X,-12}}{B_2^2}\ \mathrm{erg\ cm^{-2}\ s^{-1}}. \quad (12)$$

The single neutrino detection of IC-200107A corresponds to an approximate neutrino energy flux of $F_\nu^{\rm obs} \sim 10^{-11}$ erg cm^{-2} s^{-1} (Section 2.5). Accounting for a possible Eddington bias due to the large number of potentially similar blazars from which no neutrinos have been detected (Strotjohann et al. 2019), the actual neutrino flux from this individual source may, however, be up to a factor of ∼100 lower than the estimate provided above. Therefore, we base our estimates below on a neutrino flux of $F_\nu \sim 10^{-13}\,F_{\nu,-13}$ erg cm^{-2} s^{-1}. Thus, Equation (12) translates into a limit on the comoving target photon field energy density of

$$u'_t \gtrsim 6.8 \times 10^{-2} \frac{B_2^2\,F_{\nu,-13}}{F_{X,-12}\ln(3.1\,E_{14})}\ \mathrm{erg\ cm^{-3}}. \quad (13)$$

In the following, we will discuss the implications for the nature of such a target photon field.

4.5. Implications for the Target Photon Fields

We will distinguish two possible scenarios, which can be thought of as extreme limiting cases: (a) a target photon field that is comoving with the emission region (such as the electron synchrotron emission) or (b) a stationary target photon field in the AGN rest frame.

4.5.1. Comoving Target Photon Field

If the target photon field is comoving (e.g., the electron synchrotron photon field, which is routinely used in leptohadronic blazar models as targets for photopion production), the

target photon energy E_t' corresponds to an observed photon energy of $E_{\rm t,\ obs} \geqslant 16\, D_1^2\, \xi_{0.05}/E_{14}$ keV (i.e., hard X-rays). The directly observed X-ray flux corresponding to the comoving radiation energy density from Equation (13) is, in this case, Doppler boosted by a factor of D^4 with respect to the observer, yielding a lower limit on the X-ray flux from this radiation field of

$$F_t^{\rm obs,a} \sim \frac{D^4\, R^2\, c\, u_t'}{d_L^2}$$
$$\gtrsim 2.2 \times 10^{-11}\, \frac{F_{\nu,-13}\, R_{16}^2\, B_2^2\, D_1^4}{F_{X,-12}\, \ln(3.1\, E_{14})}\ {\rm erg\ cm^{-2}\ s^{-1}}. \quad (14)$$

Thus, a slightly smaller emission region size than 10^{16} cm, a magnetic field of $B < 10^2$ G, and/or a slightly smaller Doppler factor of $D < 10$ might plausibly allow this estimate to not overpredict the observed X-ray flux of $F_X \sim 3 \times 10^{-12}$ erg cm^{-2} s^{-1}. This is contrary to the case of TXS 0506+056, where the comoving electron synchrotron radiation field being the dominant target photon field for photopion production to produce a significant flux of VHE neutrinos could be safely ruled out (see, e.g., Keivani et al. 2018; Reimer et al. 2019; Rodrigues et al. 2019; Zhang et al. 2020).

4.5.2. Stationary Photon Field in the AGN Rest Frame

In the case of a photon field that is stationary (and quasi-isotropic) in the AGN rest frame, the external (stationary) target photon field is Doppler boosted into the blob frame, so that $E_{\rm t,\ obs} \geqslant 0.16 \xi_{0.05}/E_{14}$ keV (i.e., UV-to-soft X-rays). In this case, the target photon density is enhanced in the comoving frame compared to the AGN rest-frame energy density $u_t^{\rm AGN} \sim u_t'/\Gamma^2$. Assuming that the target photon field originates in a larger region of size $R_t = 10^{17}\, R_{t,17}$ cm surrounding the jet, the resulting directly observable UV–soft X-ray flux amounts to

$$F_t^{\rm obs,\ b} \sim \frac{u_t'\, R_t^2\, c}{\Gamma^2\, d_L^2}$$
$$\gtrsim 2.2 \times 10^{-15}\, \frac{F_{\nu,-13}\, R_{t,17}^2\, B_2^2}{\Gamma_1^2\, F_{X,-12}\, \ln(3.1\, E_{14})}\ {\rm erg\ cm^{-2}\ s^{-1}}. \quad (15)$$

For most plausible parameter choices, this remains of the order of the observed X-ray flux.

We therefore conclude that a scenario involving a dominant external radiation field as the target for photohadronic neutrino production in the jet of BZB J0955+3551 can more easily satisfy all observational constraints. However, a comoving target photon field (e.g., electron synchrotron) cannot be ruled out or even strongly disfavored.

Using the 3σ upper limit on $L_{\rm BLR}$ derived in Section 4.1, we can determine whether the external photon field needed for neutrino production (Equation (13)) could originate from the BLR of BZB J0955+3551. Assuming that the emission region is located within a spherical BLR of radius $R_{\rm BLR}$, the comoving frame BLR energy density can be written as follows:

$$u_{\rm BLR}' \sim \frac{\Gamma^2 L_{\rm BLR}}{4\pi R_{\rm BLR}^2\, c}. \quad (16)$$

Adopting $R_{\rm BLR} = R_t \sim 10^{17}$ cm and $\Gamma = 10$, we get $u_{\rm BLR}' \lesssim 0.72$ erg cm^{-3}. This implies that the BLR could act as a reservoir of seed photons for photohadronic neutrino production. However, since a definite value of $L_{\rm BLR}$ could not be ascertained, a strong conclusion cannot be made. Indeed, if we consider the disk luminosity–BLR radius relationship (see, e.g., Tavecchio & Ghisellini 2008), a low level of accretion luminosity of BZB J0955+3551 indicates a small $R_{\rm BLR}$, and, on average, the emission region would be located farther away, as also reported in various blazar population studies (see, e.g., Paliya et al. 2017, 2019b). In the absence of a strong photon field, relativistic electrons can reach up to VHEs, leading to the observation of a high synchrotron peaked SED (see Ghisellini et al. 2013). Therefore, though plausible, a BLR origin of the external photon field cannot be ascertained with high confidence.

In the following, we will further investigate the possibility of photohadronic neutrino production in BZB J0955+3551 with an external target photon field and check whether the observed optical–UV–X-ray spectrum is consistent with constraints from electromagnetic cascades initiated by the neutrino-producing pion and muon decay processes.

4.6. Numerical Simulations

Following the analytical considerations in the previous subsections, we now attempt to reproduce the observed neutrino flux with a detailed numerical model while not overshooting the observed emission. We employ the steady-state, single-zone leptohadronic model described in Böttcher et al. (2013), using parameters in agreement with the limits derived from the analytical estimates in the previous subsection. In the numerical simulation, as described in Böttcher et al. (2013), the code determines the radiating proton spectrum by evaluating an equilibrium between injection of a power-law proton spectrum, escape, and radiative cooling. The escape timescale has been set as a multiple $\eta_{\rm esc} = 30$ times the light-crossing timescale, i.e., $t_{\rm esc}' = \eta_{\rm esc} * R/c$ (in the comoving frame of the emission region). This is the same for electrons and protons. Numerically, therefore, a proton escape timescale of $t_{\rm esc}' = 10^7$ s was used in the simulation. The external photon field required for photohadronic neutrino production is represented by an equivalent electron synchrotron radiation field with the same characteristics as the presumed external radiation field in the comoving frame of the neutrino emission region, because the code of Böttcher et al. (2013) does not currently include external radiation fields for photopion production. It has been shown that the anisotropy of the target photon field has a negligible effect on the neutrino production and electromagnetic radiation output.[10] Thus, our equivalent electron synchrotron radiation setup is an appropriate proxy for the required external target photon field.

The results of the simulation reproducing the Eddington bias–corrected neutrino flux of $F_\nu \sim 10^{-13}$ erg cm^{-2} s^{-1} are shown in Figure 3 with red and magenta solid lines. The corresponding parameters are listed in Table 2. The choice of the SED parameters was based on the typical values found in previous leptohadronic modeling of blazars (Böttcher et al. 2013; Keivani et al. 2018; Reimer et al. 2019; Rodrigues et al. 2019). The very intense target photon field provides a very high $\gamma\gamma$ opacity for γ-rays in the Fermi-LAT energy range and higher, analogous to what was found for TXS 0506+056

[10] https://indico.cern.ch/event/828038/contributions/3590902/

Table 2
Parameters Used/Derived from the Numerical Simulation

Parameter	Value
Comoving photon field energy density (erg cm^{-3})	55
Comoving photon field peak frequency (Hz)	3.5×10^{17}
Magnetic field (G)	100
Bulk Lorentz factor	10
Emission region radius (cm)	1×10^{16}
Viewing angle (deg)	5.7
Low-energy cutoff of proton spectrum (GeV)	1
Proton high-energy cutoff (GeV)	10^6
Proton injection spectral index	1.1
Kinetic luminosity in protons (erg s^{-1})	1×10^{49}
Magnetic jet power (erg s^{-1})	3.75×10^{47}

Note. The shape of the proton spectrum is adopted as a power law.

(Reimer et al. 2019). This suggests that one would not expect a significant correlation between neutrino and γ-ray activity. Furthermore, the cascade synchrotron flux is well below the observed optical–UV–X-ray flux, suggesting that all electromagnetic flux components are likely to be produced by different processes and possibly even in a different emission region than the neutrino flux.

The dashed model curves in Figure 3 show an attempt to reproduce the neutrino flux of 10^{-11} erg cm^{-2} s^{-1}, i.e., neglecting the Eddington bias. For this purpose, the target photon density was increased by a factor of 36 with respect to the previous simulation, leaving all other parameters unchanged. It is obvious that, in this case, the electromagnetic output from proton synchrotron and cascades overshoots the optical–UV fluxes, and its spectral shape is very different from the observed optical–X-ray spectrum of BZB J0955+3551. This can, therefore, be ruled out.

Overall, our results suggest a scenario in which a relativistic proton population responsible for the observed neutrino emission from BZB J0955+3551 may only make a subdominant contribution to the observed X-ray flare. The detection of rapid X-ray flux variability also hints that the neutrino-producing region may not be same as the one emitting X-rays. Therefore, we argue that the detection of an X-ray flare from BZB J0955+3551 found close in time to IC-200107A is likely a coincidence, and the two events may not be physically connected.

A comprehensive analysis of the this neutrino event has also been carried out by Petropoulou et al. (2020), who studied the same event using various leptohadronic models with different emission region conditions. Though cospatial neutrino and electromagnetic radiation–producing regions were considered, the neutrino emission was not found to be related to the observed X-ray flare. These results are aligned with our findings derived from analytical calculation and a crude numerical simulation as discussed above. Moreover, among various theoretical models, they also explored a case of a hidden external photon field (a putative weak BLR) providing seed photons for photohadronic production of neutrinos. In this single-zone leptohadronic model with an external photon field, they reported that the predicted neutrino flux would be even lower during the X-ray flare to avoid overshooting the observed γ-ray spectrum (see Petropoulou et al. 2020 for details). These findings are in agreement with those reported in this work.

5. Summary

We have followed the X-ray flaring activity of BZB J0955+3551 (Giommi et al. 2020; Krauss et al. 2020) with NuSTAR, Swift, and GTC and also used the simultaneous observation from NICER. Using the high-quality OSIRIS spectrum, we determined the spectroscopic redshift of the blazar as $z = 0.55703^{+0.00033}_{-0.00021}$. On the other hand, we could not ascertain the nature of the companion object identified $\sim 3''$ southeast of BZB J0955+3551 in the i'-filter Pan-STARRS image. From the stellar velocity dispersion measured using `pPXF`, the central black hole mass of BZB J0955+3551 was derived as $10^{8.90\pm0.16}\ M_{\odot}$. Moreover, the optical spectrum of the source reveals a faint [O II] 3727 emission line with a rest-frame equivalent width of 0.15 ± 0.05 Å. We estimated a very low level of accretion activity, which is consistent with that expected from BL Lacs. There is tentative evidence ($\lesssim 3.5\sigma$) for the hour-scale flux variability in the X-ray band, as estimated from the NuSTAR and NICER light curves. Finally, we showed that a scenario involving an external photon field as a target for photopion production of neutrinos is more easily able to satisfy all observational constraints, but a scenario invoking a comoving target photon field (e.g., electron synchrotron) cannot be ruled out or even strongly disfavored. Any electromagnetic signatures of the photopion processes responsible for the neutrino emission are likely to only make a subdominant contribution to the observed electromagnetic radiation from IR to γ-rays, suggesting that the X-ray flaring event may not be directly connected with IC-200107A.

Thanks are due to the journal referee for constructive criticism. We thank T. Glauch and F. Oikonomou for fruitful discussions on the interpretation of neutrino alerts. This work was supported by the Initiative and Networking Fund of the Helmholtz Association. We are thankful to the NuSTAR and Swift PIs for approving our DDT requests and the mission operations team for quickly scheduling the observations. Thanks are also due to the NICER PI for observing the source as a DDT ToO. A.D. acknowledges the support of the Ramón y Cajal program from the Spanish MINECO. We are grateful to staff astronomer Antonio Cabrera at GTC for carrying out the OSIRIS observation. This work is based on observations made with the GTC telescope in the Spanish Observatorio del Roque de los Muchachos of the Instituto de Astrofísica de Canarias under Director's Discretionary Time. The work of M.B. is supported through the South African Research Chair Initiative of the National Research Foundation[11] and the Department of Science and Innovation of South Africa under SARChI Chair grant No. 64789. A.G.P. and A.O.G. acknowledge financial support from the Spanish Ministry of Economy and Competitiveness (MINECO) under grant Nos. AYA2016-75808-R and RTI2018-096188-B-I00, which are partly funded by the European Regional Development Fund (ERDF). A.O.G. also acknowledges financial support from the Comunidad de Madrid Tec2Space project S2018/NMT-4291. Part of this work is based on results provided by the ASM/RXTE teams at MIT and the RXTE SOF and GOF at NASA's GSFC.

[11] Any opinion, finding, and conclusion or recommendation expressed in this material is that of the authors, and the NRF does not accept any liability in this regard.

Software: XSPEC (Arnaud 1996), IRAF (Tody 1986, 1993), PyRAF (Science Software Branch at STScI 2012), HEAsoft (v6.26).

ORCID iDs

Vaidehi S. Paliya https://orcid.org/0000-0001-7774-5308
M. Böttcher https://orcid.org/0000-0002-8434-5692
A. Olmo-García https://orcid.org/0000-0001-7859-699X
A. Domínguez https://orcid.org/0000-0002-3433-4610
A. Gil de Paz https://orcid.org/0000-0001-6150-2854
A. Franckowiak https://orcid.org/0000-0002-5605-2219
S. Garrappa https://orcid.org/0000-0003-2403-4582

References

Aartsen, M. G., Abraham, K., Ackermann, M., et al. 2017a, ApJ, 835, 151
Aartsen, M. G., Ackermann, M., Adams, J., et al. 2015, ApJ, 807, 46
Aartsen, M. G., Ackermann, M., Adams, J., et al. 2017b, APh, 92, 30
Aartsen, M. G., Ackermann, M., Adams, J., et al. 2020, PhRvL, 124, 051103
Abdollahi, S., Acero, F., Ackermann, M., et al. 2020, ApJS, 247, 33
Arnaud, K. A. 1996, in ASP Conf. Ser. 101, Astronomical Data Analysis Software and Systems V, ed. G. H. Jacoby & J. Barnes (San Francisco, CA: ASP), 17
Berezinskii, V. S., & Grigor'eva, S. I. 1988, A&A, 199, 1
Blaufuss, E., Kintscher, T., Lu, L., & Tung, C. F. 2019, Proc. ICRC (Madison, WI), 36, 1021
Böttcher, M., Reimer, A., Sweeney, K., & Prakash, A. 2013, ApJ, 768, 54
Breeveld, A. A., Landsman, W., Holland, S. T., et al. 2011, in AIP Conf. Ser. 1358, Gamma Ray Bursts, ed. J. E. McEnery, J. L. Racusin, & N. Gehrels (Melville, NY: AIP), 373
Cappellari, M., & Emsellem, E. 2004, PASP, 116, 138
Celotti, A., Padovani, P., & Ghisellini, G. 1997, MNRAS, 286, 415
Cepa, J., Aguiar, M., Escalera, V. G., et al. 2000, Proc. SPIE, 4008, 623
Cepa, J., Aguiar-Gonzalez, M., Bland-Hawthorn, J., et al. 2003, Proc. SPIE, 4841, 1739
Chang, Y. L., Arsioli, B., Giommi, P., Padovani, P., & Brandt, C. H. 2019, A&A, 632, A77
Costamante, L., Bonnoli, G., Tavecchio, F., et al. 2018, MNRAS, 477, 4257
Costamante, L., Ghisellini, G., Giommi, P., et al. 2001, A&A, 371, 512
Domínguez, A., Primack, J. R., Rosario, D. J., et al. 2011, MNRAS, 410, 2556
Foffano, L., Prandini, E., Franceschini, A., & Paiano, S. 2019, MNRAS, 486, 1741
Francis, P. J., Hewett, P. C., Foltz, C. B., et al. 1991, ApJ, 373, 465
Franckowiak, A., Garrappa, S., Paliya, V., et al. 2020, ApJ, 893, 162
Garrappa, S., Buson, S. & Fermi-LAT Collaboration 2020, GCN, 26669, 1
Garrappa, S., Buson, S., Franckowiak, A., et al. 2019, ApJ, 880, 103
Ghisellini, G., Tavecchio, F., Foschini, L., Bonnoli, G., & Tagliaferri, G. 2013, MNRAS, 432, L66
Giommi, P., Glauch, T., & Resconi, E. 2020, ATel, 13394, 1
Giommi, P., Polenta, G., Lähteenmäki, A., et al. 2012, A&A, 541, A160
Gültekin, K., Richstone, D. O., Gebhardt, K., et al. 2009, ApJ, 698, 198
IceCube Collaboration 2020, GCN, 26655, 1
IceCube Collaboration, Aartsen, M. G., Ackermann, M., et al. 2018a, Sci, 361, eaat1378
IceCube Collaboration, Aartsen, M. G., Ackermann, M., et al. 2018b, Sci, 361, 147
Kalberla, P. M. W., Burton, W. B., Hartmann, D., et al. 2005, A&A, 440, 775
Keivani, A., Murase, K., Petropoulou, M., et al. 2018, ApJ, 864, 84
Kelner, S. R., & Aharonian, F. A. 2008, PhRvD, 78, 034013
King, D. L. 1985, ING Technical Note, 31, https://www.ing.iac.es/Astronomy/observing/manuals/ps/tech_notes/tn031.pdf
Kormendy, J., & Ho, L. C. 2013, ARA&A, 51, 511
Krauss, F., Gregoire, T., Fox, D. B., Kennea, J., & Evans, P. 2020, ATel, 13395, 1
Kronmueller, M., & Glauch, T. 2019, Proc. ICRC (Madison, WI), 36, 937
Lucarelli, F., Tavani, M., Piano, G., et al. 2019, ApJ, 870, 136
Mannheim, K., Stanev, T., & Biermann, P. L. 1992, A&A, 260, L1
Merritt, D. 1997, AJ, 114, 228
Mücke, A., Rachen, J. P., Engel, R., Protheroe, R. J., & Stanev, T. 1999, PASA, 16, 160
Murase, K. 2017, in Active Galactic Nuclei as High-Energy Neutrino Sources, ed. T. Gaisser & A. Karle (Singapore: World Scientific Publishing), 15
Padovani, P., Resconi, E., Giommi, P., Arsioli, B., & Chang, Y. L. 2016, MNRAS, 457, 3582
Paliya, V. S., Domínguez, A., Ajello, M., Franckowiak, A., & Hartmann, D. 2019a, ApJL, 882, L3
Paliya, V. S., Koss, M., Trakhtenbrot, B., et al. 2019b, ApJ, 881, 154
Paliya, V. S., Marcotulli, L., Ajello, M., et al. 2017, ApJ, 851, 33
Petropoulou, M., Dimitrakoudis, S., Padovani, P., Mastichiadis, A., & Resconi, E. 2015, MNRAS, 448, 2412
Petropoulou, M., Oikonomou, F., Mastichiadis, A., et al. 2020, ApJ, 899, 113
Planck Collaboration, Ade, P. A. R., Aghanim, N., et al. 2016, A&A, 594, A13
Reimer, A., Böttcher, M., & Buson, S. 2019, ApJ, 881, 46
Rodrigues, X., Gao, S., Fedynitch, A., Palladino, A., & Winter, W. 2019, ApJL, 874, L29
Schlafly, E. F., & Finkbeiner, D. P. 2011, ApJ, 737, 103
Science Software Branch at STScI 2012, PyRAF: Python alternative for IRAF, Astrophysics Source Code Library, ascl:1207.011
Shaw, M. S., Romani, R. W., Cotter, G., et al. 2012, ApJ, 748, 49
Stanev, T., Engel, R., Mücke, A., Protheroe, R. J., & Rachen, J. P. 2000, PhRvD, 62, 093005
Stickel, M., Padovani, P., Urry, C. M., Fried, J. W., & Kuehr, H. 1991, ApJ, 374, 431
Strotjohann, N. L., Kowalski, M., & Franckowiak, A. 2019, A&A, 622, L9
Tavecchio, F., & Ghisellini, G. 2008, MNRAS, 386, 945
Tody, D. 1986, Proc. SPIE, 627, 733
Tody, D. 1993, in ASP Conf. Ser. 52, IRAF in the Nineties, ed. R. J. Hanisch, R. J. V. Brissenden, & J. Barnes (San Francisco, CA: ASP), 173
van Dokkum, P. G. 2001, PASP, 113, 1420
Vazdekis, A., Sánchez-Blázquez, P., Falcón-Barroso, J., et al. 2010, MNRAS, 404, 1639
Zhang, B. T., Petropoulou, M., Murase, K., & Oikonomou, F. 2020, ApJ, 889, 118